Twenty-Sixth Symposium (International) on Combustion/The Combustion Institute, 1996/pp. 2269–2275

SOOT PRECURSOR MATERIAL: VISUALIZATION VIA SIMULTANEOUS LIF-LII AND CHARACTERIZATION VIA TEM

RANDALL L. VANDER WAL
Nyma@ NASA-Lewis
Cleveland, OH 44135, USA

Simultaneous combined laser-induced fluorescence and laser-induced incandescence (LIF-LII) images are presented for both a normal and inverse diffusion flame. The excitation wavelength dependence distinguishes the LIF and LII signals in images from the normal diffusion flame while the temporal decay distinguishes the signals in images of the inverse diffusion flame. Each flame presents a minimum in the combined LIF-LII intensity in a region separating the fuel pyrolysis and soot containing regions. Opacity, geometric definition, and extent of crystallinity measured through both bright and dark field transmission electron microscopy (TEM) characterizes the thermophoretically sampled material from within this minimal LIF-LII intensity region. TEM analysis reveals rather different soot processes occurring within the normal and inverse diffusion flame. In the normal diffusion flame, rapid chemical and physical coalescence of PAHs results in initial formation of soot precursor particles that are highly crystalline and evolve toward fully formed soot. In the inverse diffusion flame, rapid coalescence of pyrolysis products occurs, producing tarlike, globular structures equivalent in size to fully formed soot aggregates but with markedly less crystallinity than normal-appearing soot. These different material properties are interpreted as reflecting different relative rates of chemical and physical coalescence of fuel pyrolysis products versus carbonization. Significantly, these TEM images support qualitative photophysical arguments suggesting that, in general, this "dark" region observed in the LIF-LII images demarcates a transitional region in which a fundamental change in the material chemical/physical properties occurs between solid carbonaceous soot and condensed or gaseous molecular growth material.

Introduction

The intrinsic connection between polycyclic aromatic hydrocarbons (PAHs) and soot production within both diffusion [1–3] and premixed flames [4–7] suggests an intermediate stage or process whereby the molecular species are transformed to solid particulate matter. An early theory of soot formation held that large liquid droplets formed by rapid condensation of fuel pyrolysis products (mainly PAHs) subsequently transformed into soot [8]. Fuel pyrolysis studies in shock tubes [9], flow reactors [10], and premixed flame studies [5,11] provide varying degrees of support for this mechanism. An alternate soot-formation process begins with small (1–5 nm), individual entities called soot-precursor particles [12]. The existence of soot-precursor particles has been inferred based on light-scattering measurements in premixed flames [13], diffusion flames [14], and direct visualization via transmission electron microscopy (TEM) of sampled material in diffusion flames [12,15,16] and low-pressure premixed flames [4].

Although both soot formation mechanisms begin with the coalescence of fuel pyrolysis products, the difference between these mechanisms depends on the relative rates of subsequent mass growth versus carbonization and will be highly dependent on the combustion process. Carbonization in this context is understood to represent a complex series of chemical processes including but not limited to processes involving dehydrogenation and polymerization. In the former mechanism, soot mass growth is mainly completed before carbonization [8,10], whereas in the latter mechanism, carbonization appears to occur faster than mass growth [12,15]. Support for the latter process is based on the observations of continued growth of individual primary particles before significant agglomeration producing aggregates [14,17], the similar appearance of these individual primary particles (with diameter >10 nm) to those within soot aggregates [18], and laser microprobe mass analysis of soot-precursor particles revealing a hydrogen mole fraction similar to that of fully aged soot [12,15].

Given the critical link soot-precursor material (either as coalescing liquid droplets or soot-precursor particles) provides between molecular fuel pyrolysis products such as PAHs and carbonaceous soot, both spatial location and characterization of their chemical/physical properties is essential in understanding soot-formation and growth processes [8–12,15]. No reported measurements using in situ optical techniques have identified the spatial location of soot

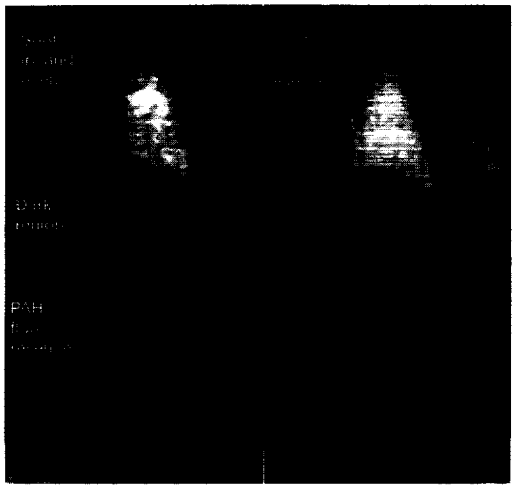

FIG. 1. (a) Simultaneous LIF-LII image of a fiber-supported burning fuel droplet (*n*-decane) produced by 266-nm excitation and (b) LII image of a similar droplet using 1064-nm excitation light. Each image was obtained 300 ms after ignition. The spatial scale is in millimeters. In each image, the droplet is spatially located just below the ruler top edge.

precursor material and characterized the material transformation processes via laser-induced fluorescence (LIF) measurements of PAHs (soot-inception species) and laser-induced incandescence (LII) measurements of soot (final product) within soot-containing diffusion flames.

Thus, the purpose of this paper is to combine LIF-LII measurements to identify the spatial location of the chemical and physical transformation of material toward solid carbonaceous material. Then this transformation is optically characterized with these optical measurements. LIF has successfully monitored PAHs within both premixed [11,13] and diffusion flames [1–3,16,19,20]. Similarly, LII has revealed soot concentrations in both one- and two-dimensional imaging configurations [21–25]. Previous combined LIF-LII measurements did not examine the transition between the LIF and LII signals along a well-defined streamline such as exists along the axial centerline of a gas-jet diffusion flame [1,24]. In this paper, simultaneous two-dimensional LIF-LII images of both a normal and inverse diffusion flame (IDF) are presented and characterized by the excitation wavelength dependence and temporal decay characteristics of the signals. The spatial identification provided by the combined LIF-LII images allows precise thermophoretic sampling measurements to be made with detailed characterization of the sampled material via both bright- and dark-field TEM.

Experimental

Light at 1064 and 266 nm was used for LII and combined LIF-LII measurements, respectively. An 8× Galilean telescope of spherical UV fused silica lenses followed by a pair of cylindrical lenses formed the laser beam into a sheet of 20 mm height. The intensity for the 1064 nm light sheet was estimated to be 2.5×10^7 W/cm^2 based on a 10 ns laser pulse and sheet thickness of 750 μm. Using a 5 ns pulse width (FWHM) and 300-μm sheet thickness for the 266-nm light yielded an approximate intensity of 9×10^6 W/cm^2. For two-dimensional images, a gated intensified camera fitted with an ultraviolet *f*4.5/105-mm (adjustable) focal length camera lens and extension tube captured the LII and/or LIF images. A bandpass filter centered at 400 nm with 70 nm FWHM bandwidth preceded the gated intensified array camera for both the LII and simultaneous LIF-LII measurements. The spatial resolution was approximately 27 pixels per millimeter. A frame grabber was used to digitize the images for transfer to the host computer.

The first flame system studied was a fiber-supported burning fuel droplet that presents a (normal) diffusion flame where the entire fuel source and pyrolysis region is enclosed within the flame front, preventing oxidative pyrolysis. The small spatial scale associated with such an envelope flame is well matched to the spatial dimensions of the TEM grid. Individual 5 μL droplets of *n*-decane ignited by a spark served as the fuel for the droplet flame. A beam block shielded the droplet from the laser light to prevent potential laser-droplet interactions.

The second flame system chosen was an inverse diffusion flame. An oxidizer flow rate of 470 sccm with an O_2/N_2 ratio of 22.5 issued from a 17-mm (i.d.) tube while a fuel-N_2 flow rate of 5.0 slpm with a C_2H_4/N_2 ratio of 0.4 flowed from a surrounding annulus of 47 mm (i.d.). Hastalloy honeycomb (0.064 cell size × 1.25 cm thick) preceded by a layer of glass beads (3 cm thick) served as flow straighteners. An outer shroud (73 mm inner ring diameter) of N_2 at roughly 25 slpm stabilized the flame and also served to dilute unburned fuel gas before venting. To eliminate the effects of room drafts, a 70 mm O.D. quartz tube fitted with slots for sampling access sat atop the outer portion of the burner. With the fuel source surrounding the central oxidizer jet, thermophoretic sampling within the fuel-rich side of the diffusion flame is readily accomplished without penetrating the flame front, thereby minimizing probe-induced disturbance of the flame. Thermophoretic sampling was accomplished using an air-actuated piston driving a rod holding the TEM grid holder and grid [26].

Observations

Figure 1a presents a simultaneous LIF-LII image of a fiber-supported burning fuel droplet using 266

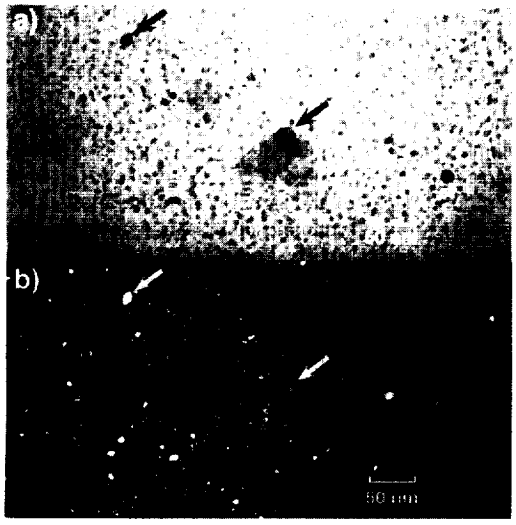

FIG. 2. (a) Bright-field TEM and (b) dark-field TEM of thermophoretically sampled material from within the dark region illustrated in Fig. 1a. The markers indicate common reference points in each panel.

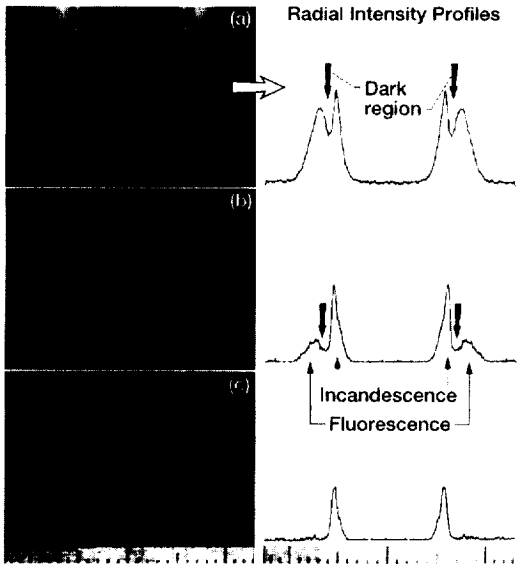

FIG. 3. Simultaneous LIF-LII images of an inverse diffusion flame of C_2H_4 with radial intensity profiles obtained at a height of 13.5 mm above the burner. The spatial scale is in millimeters. Ten individual LIF-LII images were averaged together to obtain the panels shown in the figure. Each image was obtained using the same camera intensifier gain and gate duration. The different images correspond to different signal collection time delays after the excitation laser pulse and are (a) 40 ns, (b) 80 ns, and (c) 160 ns.

nm excitation light, while Fig. 1b presents a LII image obtained using 1064-nm light. This excitation wavelength dependence can be used to distinguish molecular fluorescence and soot incandescence as discussed later. The laser-induced emission (LIE) intensity in Fig. 1a decreases with increasing distance (or equivalently residence time) above the droplet, passes through a minimum, hereafter referred to as a dark region, and then increases, whereas only LIE intensity in the far wake region is seen in Fig. 1b.

Figure 2a shows a bright-field TEM image of the thermophoretically collected material from within the dark region illustrated in Fig. 1a. Numerous small, individual particles are observed. From the indicated magnification, the particle sizes range from 1–4 nm with an average size of 3 nm. Figure 2b shows the corresponding dark-field image of the same material shown in Fig. 1a. The dark-field TEM image shows that each individual particle consists of two to three bright points, hereafter referred to as crystallites.

Figure 3 shows a sequence of LIF-LII images of the inverse diffusion flame along with radial intensity profiles where for each image, the burner surface lies 1 mm below the lower edge of the image. As shown by both the images and the corresponding radial intensity profiles (corresponding to the arrow location in Fig. 3a); a minimum in the LIE intensity exists between the inner and outer annular regions. Similar to the droplet flame, this minimum in the combined LIF-LII intensity is also hereafter referred to as the dark region.

Figure 4a shows a bright-field TEM image of thermophoretically sampled material from within the dark region of Fig. 3. The low magnification provides an overview of the material variation along the indicated radial direction within the flame. Figure 4b shows a higher magnification of material seen in Fig. 4a. A distinct contrast in both the shape definition and opacity to the electron beam is observed between the two structures shown in Fig. 4b. Interestingly, while the less-opaque object seems to possess a larger diameter than the other structure, it appears more transparent to the electron beam despite presenting more material in the electron beam path. Figure 4c shows the corresponding dark-field TEM image of the structures seen in Fig. 4b. The more-opaque structure in the bright-field image contains many more crystallites in the dark-field image compared to the other structure. The fuzziness surrounding the less-bright object is not due to focusing (both structures lie within 200 nm of each other) but represents less-dense or less-crystalline material.

Discussion

LIF-LII Signals

Both the excitation wavelength dependence and radiative lifetime distinguish the LIF signal from the

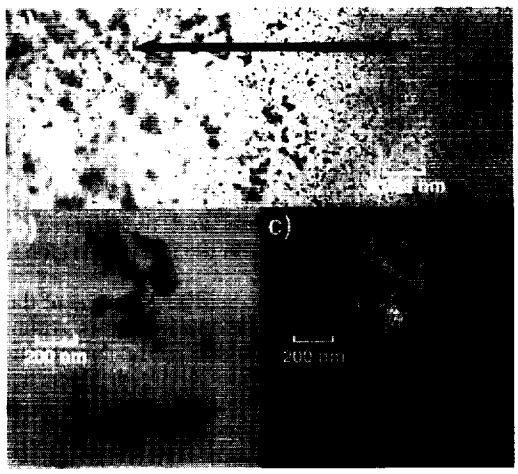

FIG. 4. (a) Bright-field TEM at low magnification illustrating the variation in soot morphology across the soot-containing region. The arrow is directed radially outward. The image is meant to convey the range of particle morphologies observed. (b) Bright-field TEM contrasting the soot morphologies observed in (a). (c) Dark-field TEM of the corresponding structures observed in (b). For each image, the sampling height was 13.5 mm above the burner.

LII signal in the images in Figs. 1 and 3, respectively. Light at 1064 nm will not produce molecular fluorescence in the visible, whereas 266 nm light is known to readily excite electronic transitions in a variety of combustion intermediates resulting in fluorescence [27,28]. To excite visible fluorescence, multiphoton absorption of 1064 nm light that could occur through a nonresonant multiphoton absorption process is necessary. Not only is infrared multiphoton absorption improbable given the laser intensities used, but even if it did occur, it would likely result in molecular dissociation from the ground electronic state, which generally does not lead to photofragment emission [29]. Thus, the presence of signal in the near-wake region using 266 nm excitation and its absence when using 1064-nm light indicates that this signal is LIF, likely arising from PAH fluorescence. Since both 1064 and 266 nm light is readily absorbed by soot, at sufficient intensities, each excitation wavelength is capable of producing LII [16]. Thus, the similar spatial extent of the laser-induced emission signal in the far-wake region of Figs. 1a and 1b using either 266 or 1064 nm light indicates that this LIE signal is LII.

While fluorescence from PAHs within diffusion flames is generally detectable only tens of nanoseconds after laser excitation [3,16], LII is detectable hundreds of nanoseconds after the laser pulse at moderate laser intensities [16,21–25]. The slower temporal decay of LII compared to fluorescence results from cooling processes, which determine the LII signal decay, being slower than collisional quenching, which determines the fluorescence decay rate within atmospheric pressure flames [16]. Thus, the rapid temporal decay of the LIE signal in the outer annular region of the inverse diffusion flame shown in Fig. 3 indicates that this signal is molecular fluorescence (LIF). Conversely, the long temporal decay of the signal within the annular extending hundreds of nanoseconds (in contrast to tens of nanoseconds for the fluorescence) confirms the identity of this signal as soot incandescence (LII).

TEM Images

Droplet

The small size (1–4 nm) of the particles seen in Fig. 2a is characteristic of those observed by other researchers as indicating the first incipient soot particles [4,12,15,16]. The intermediate spatial location of these particles between the PAH- and soot-containing regions confirms the transitional role of soot-precursor particles in the soot-formation process. At slightly higher axial heights within the dark region shown in Fig. 1a, larger individual particles of greater than 5 nm diameter were found, indicating further mass growth.

Despite their small size and close temporal origin to molecular PAHs, the soot-precursor particles observed in Fig. 2 are crystallized. The bright points in the dark-field TEM image of Fig. 2b are interpreted as crystallites appropriately oriented to diffract a portion of the electron beam into the viewing angle. In fully formed carbon black particles, X-ray diffraction has shown each particle to be made up of a large number of crystallites ($\sim 10^{+4}$) [30]. Each crystallite consists of 5–10 sheets of carbon atoms with each sheet having a length or breadth of 20–30 Å. A random packing of such crystallites is commonly considered amorphous carbon [30]. Diffraction from ordered carbon layer planes indicates carbonization of these precursor particles has occurred, with the chemical/physical structure no longer resembling a "clump" of condensed hydrocarbons but rather a disorganized solid. Such a rapid material transformation is feasible because LMMA analysis of soot precursor particles collected within an ethylene-air diffusion flame indicates that graphitization of soot-precursor particles can occur rapidly, ($\sim$10 ms), resulting in a particle hydrogen mole fraction, X_H, of 0.15, typical of mature soot released from flames [12]. As the transparency of these structures increased in the bright field TEM images, the number of crystallites within these structures decreased, as observed in the dark-field TEM images. In summary, these results indicate that carbonization proceeds rapidly compared to mass growth for the soot-precursor particles in the droplet flame.

Inverse Diffusion Flame

Numerous soot-formation/growth studies have used shock tubes [9,31,32], flow reactors [8,10], and *in situ* probe sampling within premixed [4–7] and diffusion flames [2,20,33]. With the exception of the carbon black industry, few fuel pyrolysis studies have used TEM for product morphological analysis. One particularly revealing study, however, sampled the exhaust within a flow tube reactor of 2% benzene in N_2 at 1383 K at different positions (residence times) [10]. With increasing residence time, the rapid decrease in the extractable tar content coincided with an equally rapid increase in the carbonaceous residue content of the sampled material. TEM micrographs of the sampled material at early residence times (<50 ms) revealed a condensed phase of semitransparent tarlike material existing in large "globs," far different than the usual chainlike structures normally associated with soot. Hereafter, the term *tar-like* is used to denote a disorganized, unstructured solid material (potentially a highly viscous "liquid" at flame temperatures) with both a lower degree of crystallinity and C/H ratio compared to ordinary soot commonly observed.

The TEM observations in the inverse diffusion flame shown in Fig. 4 are consistent with these results. As seen in the bright-field TEM image of Fig. 4b, the decreased opacity despite the larger size indicates that the tar-like material appears less dense to the electron beam. The relatively uniform opacity of the tarlike material suggests a rather uniform composition. Far less crystallinity of the tarlike substance is revealed by the markedly lower intensity in the dark-field TEM image of Fig. 4c compared to the normal-appearing soot aggregate. The chainlike resemblance of the tar-like substance indicates that agglomeration of the pyrolytic material has occurred before carbonization [8,10]. The poorer geometrical outline is consistent with the formation of the tarlike aggregate via pyrolytic deposition.

Just as for normal diffusion flames, the fuel-rich side of the inverse diffusion flame closely resembles a pyrolytic system with the flame front presenting an oxygen barrier. In this context, the present results indicate that rapid deposition of pyrolytic material (mass growth) occurs before significant carbonization [8,10]. This accounts for the rather uniform tarlike appearance of the structures shown in Fig. 4, the lack of opacity in the bright-field TEM images (Figs. 4a and 4b), and the lack of crystallinity in the dark-field TEM image (Fig. 4c). While the images in Fig. 4 do not prove soot formation occurring via carbonization of large tar-like structures, they do indicate that significantly different relative rates of soot-precursor material nucleation, coalescence, and growth occur relative to carbonization in this flame system compared to the droplet flame (normal diffusion flame), resulting in very different material properties compared to normal carbonaceous soot as discussed next.

The Dark Region

As seen in Figs. 1a and 3, a minimum occurs in the combined LIF and LII intensity spatially located between the PAH- and soot-containing regions. The fluorescence intensity decrease is likely due to three factors: (a) an increase in the size of PAHs through molecular growth, (b) a decrease in the gas-phase PAH concentration, and (c) PAH coalescence into soot-precursor particles. As PAHs grow in size, the number of rovibrational and electronic quantum states increases dramatically [34]. With an increased quantum state density, nonradiative transitions between electronic states increases because of increased coupling between these states [34]. Thus, the fluorescence quantum yield decreases. Secondly, as the PAHs coalesce into particles, the gas-phase number concentration of PAHs decreases since large PAHs presumably serve as building blocks for soot-precursor particles, while small PAHs serve as initial mass growth material for the precursor particles [35,36]. Thirdly, as carbonization continues, the PAH "molecules" lose their individual identity and become assimilated into an object that is becoming more solid in form. With increasing solid structure, the probability for nonradiative decay increases dramatically because of the far higher quantum state density [37]. Thus, while the particle readily absorbs light and may still fluoresce because the constituent "molecules" possess highly absorbing chromophoric groups, with increasing carbonization, the fluorescence quantum yield decreases relative to isolated gas-phase molecules, eventually becoming negligible. These three factors account for the decrease in fluorescence intensity with increasing axial height seen in Fig. 1a. Similarly, the probability for nonradiative decay is greatly increased in condensed and/or partially carbonized tar-like material relative to gaseous species, thus accounting for the fluorescence intensity decrease with decreasing radial distance seen in Fig. 3.

With increasing solid character of the particle, rapid internal dissipation of energy deposited through multiphoton absorption occurs [38]. If a sufficient number of photons is absorbed, the particle will be heated to incandescence temperatures. The detailed chemical and physical structure of the particle will determine the fate of the particle upon rapid, high-energy deposition. Very small soot-precursor particles are thought to possess a high number of reactive radical sites accounting for the rapid mass growth [35]. This large number of reactive sites indicates that the extent of bonding of the aromatic structures within the compound is very incomplete. Upon rapid energy deposition, bonds linking aromatic units to the solid structure may sever, leading

to fragmentation. Until bonding of adjoining molecular units is substantially complete, fragmentation of the particle will likely occur during the energy deposition process, resulting in minimal or no incandescence. Similarly, the tar-like objects that are only partially carbonized may be intermediate between molecular and solid structures [9–11,32]. If enough energy accumulates within the particle through absorption of multiple photons (not necessarily simultaneously), molecular fragmentation rather than incandescence would more likely occur given the largely molecular structure. Thus, during this transitional period in which significant chemical and physical material transformation processes are occurring, both nonradiative transitions and/or fragmentation are likely to result from laser excitation. Consequently, minimal intensity is observed in either the LIF or LII signals, thereby accounting for the dark region observed in the simultaneous LIF-LII images.

These changes in the photophysical properties reflect the chemical and physical transformation in material properties occurring between molecular material (condensed or gaseous) and solid carbonaceous soot. This transformation appears general despite the very different apparent relative rates of soot-precursor material growth and coalescence versus carbonization within the normal and inverse diffusion flames. Both the decreasing opacity with increasing radial distance (or increasing tar-like appearance) of the soot structures seen in the bright-field TEM images of Figs. 4a and 4b and decreasing crystallinity seen in the dark-field TEM image of Fig. 4c reveal a consistent physical/chemical change in the material composition. With increasing radial distance from the centerline in the inverse diffusion flame, the material changes from a disorganized yet highly crystalline solid to barely visible condensed molecular matter. A similar material transformation is suggested by the soot-precursor particles observed in Fig. 2. In contrast to the large structures observed in Fig. 4, the initial small structures and subsequent growth suggest a soot-formation process proceeding through chemical and physical condensation of large molecules (PAHs) followed by mass addition concurrent with carbonization. Irrespective of the relative rates, surface mass growth, coalescence, and carbonization are all critical processes leading to solid carbonaceous soot.

The observed optical properties of the soot structures also vary in a spatially similar manner. With decreasing radial distance, the LIF intensity (with no apparent contributing LII signal) decreases from a maximum reaching a minimum spatially overlapped with an intensity minimum in the LII signal as seen in Fig. 3. At smaller radial distances, the LII intensity increases, reaching a maximum still on the fuel-rich side of the diffusion flame. Analogous behavior is observed in the normal diffusion flame with increasing axial distance above the burning droplet. At small axial heights within the normal diffusion flame and large radial distances within the IDF, no material was collected via thermophoretic sampling as would be expected if only gaseous species were present. In these regions, only fluorescence is observed. At high axial heights in the normal diffusion flame or small radial distances in the IDF flame, only solid carbonaceous soot was found through TEM analysis of thermophoretically sampled material. In these regions, only incandescence is observed.

Thus, the postulated variation in material photophysical properties suggested by the spatial variation in the LIF and LII intensities is supported by the spatial variation in the material composition as revealed by both the bright- and dark-field TEM images. Most significantly, the minimum in the combined LIF-LII intensities is indicative of the chemical and physical changes accompanying the transformation of molecular matter into solid carbonaceous soot regardless of the specific soot formation route. On this basis, the dark region illustrated in the simultaneous LIF-LII images spatially locates the region containing soot-precursor material.

Conclusions

Simultaneous LIF-LII images are valuable for visualizing both PAH and soot-containing regions within both transitory (droplet) flame and steady-state IDF flames. The LIF and LII signals may be distinguished either by the excitation wavelength dependence or the temporal decay following the laser pulse. As revealed in the LIF-LII images, a dark region appears juxtaposed between the PAH and soot-containing regions. TEM measurements of thermophoretically sampled material from within this dark region suggest very different rates of soot-precursor material growth and coalescence versus carbonization within the normal and inverse diffusion flame. Postulated photophysical properties accounting for the minimal LIF and LII intensity (the "dark" region) observed in the LIF-LII images are supported by both bright- and dark-field TEM measurements of the sampled material. Both the spatial position of the dark region and TEM measurements indicate that the dark region represents a transformation region. In this region, the chemical and physical material conversion between gaseous or condensed molecular species (soot-precursor material) and solid carbonaceous soot particles occurs.

Acknowledgments

Support under NASA contract NAS3-27186 with Nyma Inc. for this work is acknowledged. The author extends special thanks to Mr. David Hull of NASA-LeRC for perform-

ing the TEM measurements and for helpful discussions regarding TEM.

REFERENCES

1. Ni, T., Gupta, S. B., and Santoro, R. J., *Twenty-Fifth Symposium (International) on Combustion*, The Combustion Institute, Pittsburgh, 1994, pp. 585–592.
2. Prado, G., Garo, A., Ko, A., and Sarofim, A., *Twentieth Symposium (International) on Combustion*, The Combustion Institute, Pittsburgh, 1984, pp. 989–996.
3. Gomez, A., Littman, M. G., and Glassman, I., *Combust. Flame* 70:225–241 (1987).
4. Wersborg, B. L., Fox, L. K., and Howard, J. B., *Combust. Flame* 24:1–10 (1975).
5. Ciajolo, A., D'Anna, A., Barbella, R., and Tregrossi, A., *Twenty-Fifth Symposium (International) on Combustion*, The Combustion Institute, Pittsburgh, 1994, pp. 679–685.
6. Bittner, J. D. and Howard, J. B., *Eighteenth Symposium (International) on Combustion*, The Combustion Institute, Pittsburgh, 1981, pp. 1105–1116.
7. McKinnon, J. T. and Howard, J. B., *Twenty-Fourth Symposium (International) on Combustion*, The Combustion Institute, Pittsburgh, 1994, pp. 965–972.
8. Lahaye, J. and Prado, G., *Carbon* 12:24–31 (1974).
9. Graham, S. C., Homer, J. B., and Rosenfeld, J. L. J., *Proc. R. Soc. London, Ser. A* 344:259–285 (1975).
10. Lahaye, J., in *Particulate Carbon Formation during Combustion*, (Siegla, D. C. and Smith, G. W., Eds.), Plenum Press, New York, 1981, p. 143.
11. D'Alessio, A., Gambi, G., Minutolo, P., Russo, S., and D'Anna, A., *Twenty-Fifth Symposium (International) on Combustion*, The Combustion Institute, Pittsburgh, 1994, pp. 645–651.
12. Dobbins, R. A., Fletcher, R. A., and Lu, W., *Combust. Flame* 100:301–309 (1995).
13. Haynes, B. S., Jander, H., and Wagner, H. G., *Ber. Bunsenges. Phys. Chem.* 84:585–592 (1980).
14. Santoro, R. J. and Semerjian, H. G., *Twentieth Symposium (International) on Combustion*, The Combustion Institute, Pittsburgh, 1994, pp. 997–1006.
15. Dobins, R. A. and Subramaniasivam, H., in *Soot Formation in Combustion*, (Bockhorn, H., Ed.), Springer Verlag, Heidelberg, 1994, p. 290.
16. Vander Wal, R. L., Jensen, K. A., and Choi, M. Y., *Combust. Flame*, 1996, accepted.
17. Megaridis, C. M. and Dobbins, R. A., *Twenty-Second Symposium (International) on Combustion*, The Combustion Institute, Pittsburgh, 1988, pp. 353–362.
18. Megaridis, C. M. and Dobbins, R. A., *Combust. Sci. Technol.* 71:95–109 (1990).
19. Petarca, L. and Marconi, F., *Combust. Flame* 78:308–325 (1989).
20. Smyth, K. C., Miller, J. H., Dorfman, R. C., Mallard, W. G., and Santoro, R. J., *Combust. Flame* 62:157–181 (1985).
21. Vander Wal, R. L. and Weiland, K. J., *J. Appl. Phys. B* 59:445–454 (1994).
22. Vander Wal, R. L. and Dietrich, D. L., *Appl. Opt.* 34:1101–1107 (1995).
23. Shaddix, C. E., Harrington, J. E., and Smyth, K. C., *Combust. Flame* 99:723–732 (1995).
24. Cignoli, F., Benecchi, S., and Zizak, G., *Appl. Opt.* 33:5778–5782 (1994).
25. Ni, T., Pinson, J. A., Gupta, S., and Santoro, R. J., *Appl. Opt.* 34:7083–7091 (1995).
26. Vander Wal, R. L., Choi, M. Y., and Lee, K.-O., *Combust. Flame* 102:200–204 (1995).
27. Bengtsson, P.-E. and Alden, M., *Combust. Sci. Technol.* 77:307–318 (1991).
28. Beretta, F., D'Alessio, A., D'Orsi, A., and Minutolo, P., *Combust. Sci. Technol.* 85:455–470 (1992).
29. Letokhov, V. S., *Nonlinear Laser Chemistry: IRMPD*, Bristol, New York, 1985.
30. Palmer, H. B. and Cullis, C. F., in *Chemistry and Physics of Carbon*, Vol. 1 (Walker, P. L., Ed.), Marcel Dekker, New York, 1965, p. 265 (and references therein).
31. Frenklach, M., Taki, S., and Matula, R. A., *Combust. Flame* 49:275–282 (1983).
32. Graham, S. C., *Sixteenth Symposium (International) on Combustion*, The Combustion Institute, Pittsburgh, 1976, pp. 663–669.
33. Hepp, H., Siegmann, K., and Sattler, K., *Chem. Phys. Lett.* 233:16–22 (1995).
34. Steinfeld, J. I., *Molecules and Radiation: An Introduction to Modern Molecular Spectroscopy*, The MIT Press, Cambridge, 1981, pp. 169–225.
35. Howard, J. B., *Twenty-Third Symposium (International) on Combustion*, The Combustion Institute, Pittsburgh, 1990, pp. 1107–1127.
36. Marr, J. A., Giovane, L. M., Longwell, J. P., Howard, J. B., and Lafleur, A. L., *Combust. Sci. Technol.* 101:301–309 (1994).
37. Turro, N. J., *Modern Molecular Photochemistry*, Benjamin/Cummings Menlo Park, CA, 1978, pp. 153–195.
38. Parker, S. P., Ed., *The Solid State Physics Source Book*, McGraw Hill, New York, 1988, pp. 95–198.